JMEPEG (2022) 31:105–112
https://doi.org/10.1007/s11665-021-06214-0

©ASM International
1059-9495/$19.00

Effect of Forging on Microstructure and Properties of Al-9Si-5Cu-0.2Zr-0.1Sr-0.16Ti-0.1Ce Cast Aluminum Alloy

Chen Li, Xiaojing Xu, Rikai Zhang, Xiaopeng Jin, Peng Zhang, Hongbo Wei, and Yuan Zhuang

Submitted: 27 September 2020 / Revised: 14 July 2021 / Accepted: 4 August 2021 / Published online: 9 September 2021

Herein, Al-Si-Cu aluminum alloy was prepared and the effect of forging on the microstructure and mechanical properties of novel Al-9Si-5Cu-0.2Zr-0.1Sr-0.16Ti-0.1Ce cast aluminum alloy was investigated. The microstructure analyses show that after forging, the casting defects disappeared, and the irregular Si-eutectic was spheroidized and randomly distributed. The coarse intermetallic compounds (IMCs) gradually dissolved during the solution treatment, and the increased supersaturation of the matrix promoted precipitation kinetics, leading to the coexistence of dense fine θ and θ' strengthening phases. Moreover, the dislocation strengthening effect for the forged alloy was enhanced. The mechanical tests show that compared to the as-cast alloy, the mechanical properties of the forged alloy including the hardness, yield strength, tensile strength, and plasticity were improved by optimizing the microstructure.

Keywords Al-Si-Cu cast aluminum alloy, forging, mechanical properties, microstructure, plasticity

1. Introduction

The light-weight approach of automobile bodies is not only an effective way to conserve energy but also to improve the controllability and comfort level of automobiles. Hence, with the increasing demand for light-weight automobile bodies, the performance requirements for aluminum alloy parts have gradually enhanced (Ref 1–3). Traditionally, to satisfy the required mechanical properties during service, the deformed aluminum alloy (such as 6000 series) or cast aluminum alloy (like A356) has been widely used to tailor the chassis and structure parts. However, the production of 6000 series aluminum alloy in general involves a complicated process and high cost. The current mainstream Al-Si-Cu cast aluminum alloys, such as ADC10 and A380, have unsatisfactory mechanical properties because of the mutually exclusive relationship between strength and ductility. Therefore, it is challenging to develop advanced cast aluminum alloys with substantial simultaneous improvement of strength and ductility.

Due to their excellent thermal stability and casting ability, Al-Si-Cu series cast aluminum alloys have been commonly adopted in industries. The microstructure of binary Al-Si alloy constitutes primary phases of Al and Si and their eutectic phases (Ref 4), wherein the volume fraction of eutectic-Si accounts for more than 50%. The addition of Cu in the alloy may lead to formation of some intermetallic compounds (IMCs). When the Cu content in Al-Si-Cu alloy is 4.5-5.5%, a high-density of Al_2Cu phases precipitates within the Al matrix and disperses during the aging process, resulting in the strengthening effect (Ref 5). However, after casting, acicular IMCs, coarse primary crystal phases, and lath-like eutectic Si structures are distributed in the Al-Si-Cu alloy, leading to significant softening and deterioration of the mechanical properties. Moreover, casting defects, such as pores (caused by air retention), coarse dendrites, and inhomogeneous microstructure are easily introduced in the conventional casting process, leading to uneven mechanical properties of the cast alloy.

The forging process can eliminate casting defects, which optimizes the microstructure and improves its structure and mechanical properties. Moreover, the forged products have excellent mechanical properties, good surface quality, tight geometric tolerance, and closeness to the final product shape (Ref 6). Kang et al. (Ref 7, 8) reported that the semi-solid forging parts have higher ultimate tensile strength than that of the casting ones. Wu et al. (Ref 9) claimed that the grain size of the original Si for Al-Si alloy can be reduced by amplifying the pressure of liquid forging.

Herein, Al-Si-Cu aluminum alloy was developed and the effects of forging on the microstructure and mechanical properties are studied in detail. This novel Al-Si-Cu aluminum alloy displayed $>$ 380 MPa tensile strength, $>$ 10% elongation, and excellent casting properties, and the alloy is termed as Al-9Si-5Cu-0.1Sr-0.2Zr-0.16Ti-0.1Ce alloy.

2. Experimental

The cast ingot employed in this experiment was Al-9Si-5Cu-0.1Sr-0.2Zr-0.16Ti-0.1Ce aluminum alloy. Before casting, the aluminum ingot was first placed in a well-type furnace and melted to clean the furnace. Afterwards, materials including Al-Cu (50.12 wt.% Cu) alloy, Al-Si (16.03 wt.% Cu) alloy, Al-Ti-B (5.01wt.% Ti) alloy, Al-Zr (4.11 wt.% Zr) alloy, Al-Ce (10.04 wt.% Ce) alloy, and pure Al (99.97 wt.%) were placed in the

Chen Li, Xiaojing Xu, Rikai Zhang, Xiaopeng Jin, Peng Zhang, Hongbo Wei, and **Yuan Zhuang**, Institute of Advanced Manufacturing and Modern Equipment Technology, Jiangsu University, Zhenjiang, China. Contact e-mail: yjs_xx@126.com.

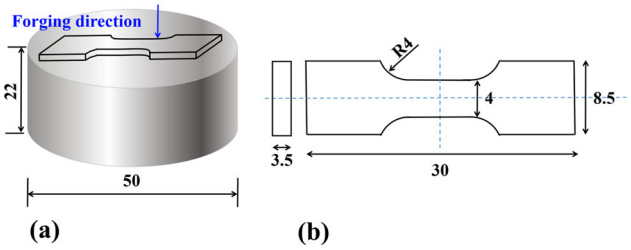

Fig. 1 (a) Diagram of sample for microstructure and strength test and (b) the schematic diagram of tensile test sample (unit: mm)

melting stove. The melting temperature was set at 850 °C for 120 min, and stirring was performed during this period. When the temperature dropped to 750 °C, hexachloroethane was inserted for degassing. After standing for 15 min, hexachloroethane was added again for secondary degassing. Next, the molten alloy was deslagged and poured into a metal mold (Φ 40 mm × 150 mm) to prepared ingot.

A RX3-30-13 resistance furnace was used for homogenization annealing (250 °C × 6 h + 350 °C × 6 h + 450 °C × 6 h + 480 °C × 20 h). After annealing, the cut aluminum alloy ingots (Φ 40 mm × 44 mm) were directly placed into the preheated mold with an inner diameter of Φ50 mm × 50 mm and forged at 450 °C using a hydraulic press at the stamping speed of 10 mm/s. The specimens were forged into a cylinder of size Φ 50 mm × 22 mm under the pressure of 100t with 50% deformation (see Fig. 1a). The subsequent heat treatment started with solution treatment (450 °C × 2 h + 460 °C × 2 h + 470 °C × 2 h), followed by water quenching and aging (120 °C × 24 h). The undeformed and forged alloys were named 1# and 2# alloys, respectively.

JEOL-JSM-IT300 scanning electron microscope (SEM) was used to observe 1# and 2# alloy samples. FEI Talos F200X transmission electron microscope (TEM) was also used to analyze the microstructure of the alloys. TEM samples were prepared by mechanical thinning and ion thinning successively (Gatan 691). The phases of alloy were examined using an AXS-D8 ADVANCE type x-ray diffractometer (XRD) (λ = 0.15406 nm, scanning speed 5°/min). The surface hardness was tested on an INNOVATEST-FALCON 500 Vickers hardness tester (25 g working load and 15 s load time) with an average of at least five readings for each value. The tensile experiments were conducted on a WDW-200g type testing machine using 20 kN force at the room temperature. The tensile test samples were acquired from the center of the cylindrical alloy (perpendicular to the extrusion direction) (see Fig. 1a). Figure 1(b) displays the geometry of the tensile test sample.

3. Results

3.1 Mechanical Properties

The mechanical properties of Al-9Si-5Cu-0.2Zr-0.1Sr-0.16Ti-0.1Ce aluminum alloys after aging are presented in Fig. 2. As shown in Fig. 2(a), the hardness, yield strength, and tensile strength of 1# alloy reached 138 HV, 133 MPa, and 372 MPa, respectively. After forging, these three values of 2# alloy were improved to 145 HV, 188 MPa and 397 MPa, respectively. According to the stress-strain curve displayed in Fig. 2(b), the elongation after fracture for 1# alloy was 6%, while the elongation for forged alloy significantly increased to 14%, which is almost twice that for 1# alloy.

Figure 3 displays the SEM images of surface fracture morphologies of 1# and 2# alloys. The fracture morphologies mainly demonstrated ductile fracture. For 1# alloy, the shrinkage holes and the coarse tearing edges were found in Fig. 3(a), which is the manifestation of brittleness. These results correspond to 6% elongation in the tensile tests. However, 2# alloy exhibited different fracture morphology; i.e., the fracture surface was relatively flat, and the coarse tearing edge and hole basically disappeared. Small and shallow dimples were evenly distributed on the surface. These phenomena signify that the ductility of 2# alloy was significantly better than that of alloy 1# (Fig. 3b).

3.2 Microstructure Characterization

Figure 4 presents the microstructure of (a-c) as-cast and (d-f) forged Al-9Si-5Cu-0.1Sr-0.2Zr-0.16Ti-0.1Ce alloy. As per Fig. 4(a), two main features were found in the cast Al-Si-Cu alloy, namely the dark gray Si-containing particles and white

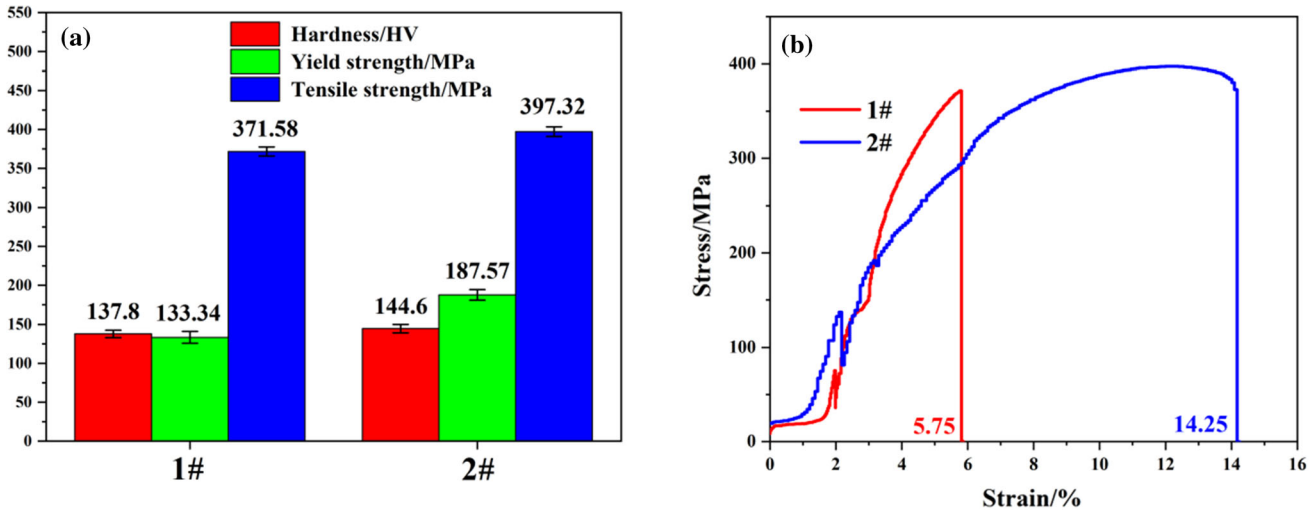

Fig. 2 Mechanical properties of 1 # and 2 # alloys: (a) hardness, yield strength, and tensile strength and (b) stress-strain curves

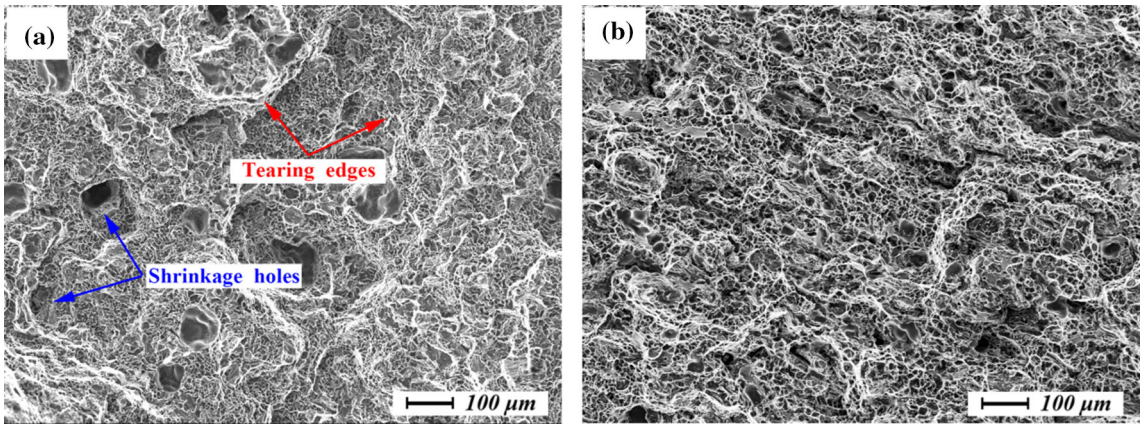

Fig. 3 SEM images of tensile fracture morphologies: (a) 1# and (b) 2# alloys

irregular non-equilibrium phases. Using Si-mapping to characterize the morphology and distribution of Si particles (Fig. 4b), the Si-phases presented rough polyhedrons and irregular slats with a size of about 3-25 μm. The backscattered electron (BSE) image in Fig. 4(c) shows that there were several white lumps and fine needles in the alloy. EDS analysis revealed that white undissolved phases such as spot a1 and a2 within the figure were Cu and Zr rich IMCs (see Table 1).

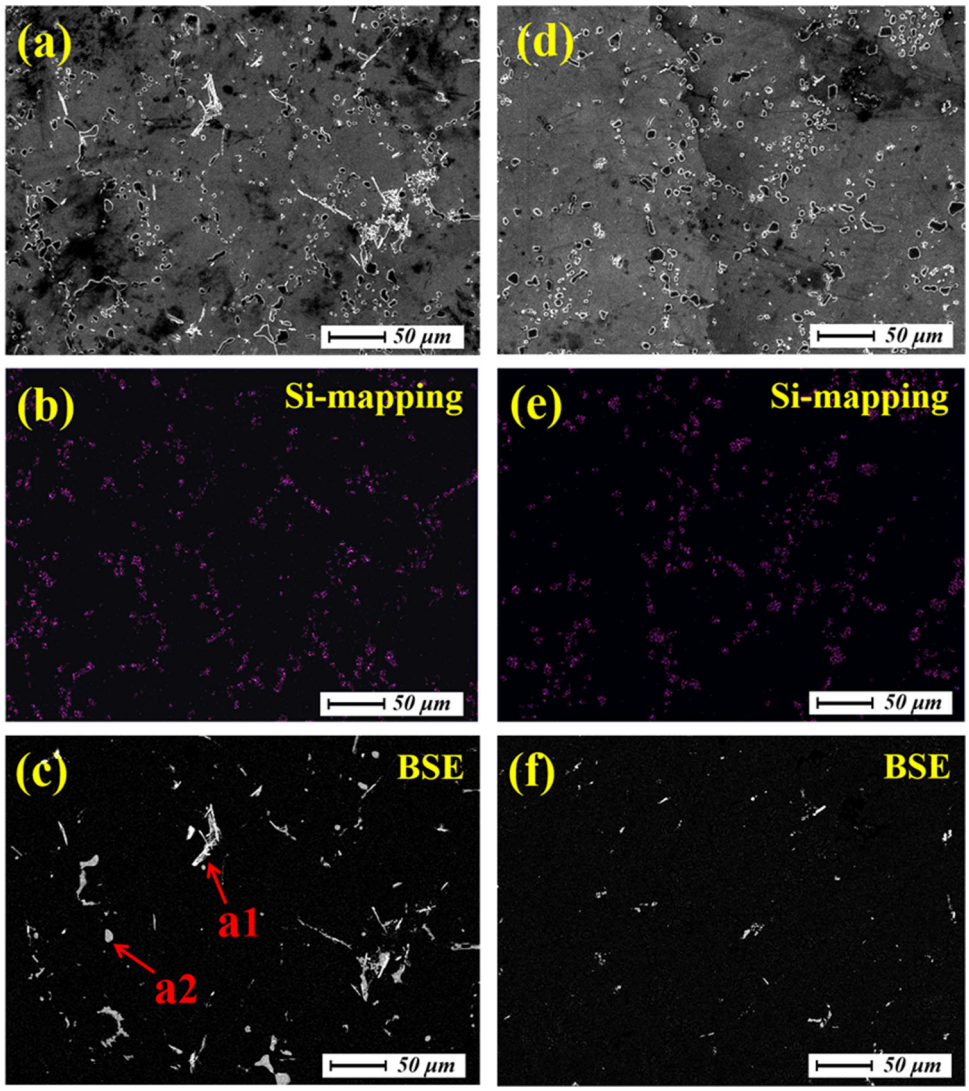

Fig. 4 SEM morphology of Al-Si-Cu alloys: (a-c) as-cast alloy and (d-f) forged alloys

Table 1 EDS analyses of particles shown in Fig. 2(c) in At.%

EDS points	Al	Si	Cu	Ti	Zr	Sr	Ce	Fe
a1	74.30	5.22	12.46	1.20	4.11	…	…	3.51
a2	71.82	1.58	15.42	…	4.61	…	…	6.57

In comparison, the forged alloy has uniform distribution of Si-containing phases (Fig. 4d, e), while the irregular slats disappeared and almost spheroidized. As per the BSE image shown in Fig. 4(f), after forging, the number of Cu and Zr rich IMCs was significantly reduced, while some IMCs were shattered. In other words, those coarse IMCs were broken into granules under forging and gradually dissolved in the matrix during subsequent solution treatment.

3.3 XRD Analysis

Figure 5 demonstrates the XRD patterns of pure aluminum (JCPDS No. 04-0787) and 1# and 2# alloys. Compared with pure aluminum and 1# alloy, the (200) peak intensity of 2# alloy was low. The diffraction pattern of 1# alloy was similar to that of pure Al, signifying that both the crystal orientation and texture of the alloy were affected by forging.

The method proposed by Williamson and Hall was used to further process the XRD data to obtain the dislocation density of aluminum alloy. The formula for the same is presented below (Ref 10, 11):

$$\rho = \frac{2\sqrt{3}(e^2)^{1/2}}{(d \times b)} \quad \text{(Eq 1)}$$

where ρ is the dislocation density, (e^2) is the lattice strain, d is the size of the XRD coherent diffraction zone, and b is the Burgers vector of aluminum (0.286 nm) (Ref 12). The unknown terms (e^2) and d in formula (1) can be obtained by formula (2) (Ref 13):

$$\frac{(\delta 2\theta)^2}{\tan^2\theta_0} = 25(e^2) + \frac{\lambda}{d}\left(\frac{\delta 2\theta}{\tan\theta_0 \sin\theta_0}\right) \quad \text{(Eq 2)}$$

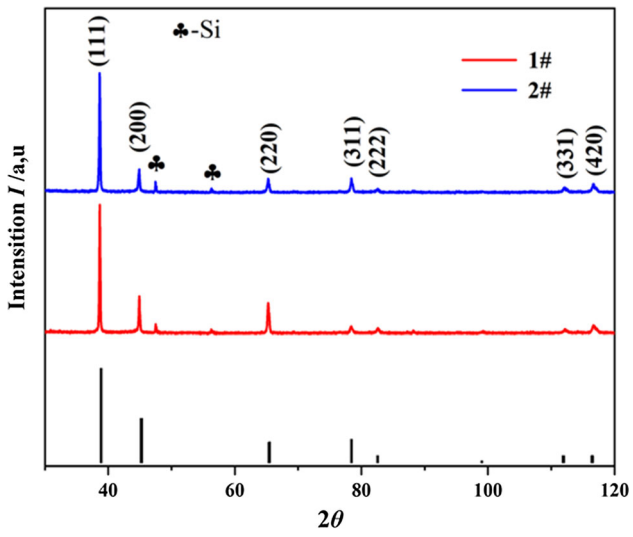

Fig. 5 XRD spectrums of pure Al, 1# and 2# alloys

where $\delta 2\theta$, θ_0, and λ are the full width at half maxima (FWHM), angle position of main diffraction peak, and wavelength, respectively. In this test, the λ value was 0.15406 nm. By loading XRD data into Jade 6.5 software, the 2θ and half peak width data for each diffraction peak were obtained (Fig. 6a, b) for 1# and 2# alloy, respectively). Using the obtained 2θ data into formula (2), the relationship between $\delta 2\theta/(\tan\theta_0 \sin\theta_0)$ and $(\delta 2\theta)^2/(\tan\theta_0)^2$ are plotted in Fig. 6(c) and (d) for 1# and 2# alloy, respectively. The effect of dislocations on strength (σ_p) and dislocation density (ρ) is given by (Ref 10):

$$\sigma_\rho = M\alpha Gb\rho^{1/2} \quad \text{(Eq 3)}$$

where M is the Taylor factor = 3.06, α is the numerical factor value of 0.24, and G is the shear modulus of 26 GPa. The calculated data of dislocation density are listed in Table 2. Compared with 1# alloy, the dislocation density and its strengthening effect of the forged alloy were significantly increased. This can be attributed to the introduction of more dislocations via deformation. The movement of dislocations in the alloy may have been hindered by the dislocation entanglement, resulting in dislocation strengthening.

3.4 TEM Analysis

Figure 7 presents the TEM image of 1# alloy. As observed from Fig. 7(a), numerous spherical Si-phases with sizes of about 100-200 nm were uniformly distributed in the alloy matrix. Also, as per high-magnification image (Fig. 7(b)), other than eutectic Si, striped and rod-like structures appeared, which are inferred as the precipitated θ phase in view of the size and morphology of the precipitate (Ref 14, 15).

For 2# alloy, the morphology and distribution of the precipitated phase are presented in Fig. 7(c). Numerous second phases were dispersed in the Al matrix, displaying needle-like and rod-like morphologies. These dispersed acicular precipitates were deduced as the metastable θ' and stable θ phases (Fig. 7d) (Ref 14–16).

The size parameters of precipitates significantly influence the mechanical properties of aluminum alloy. Therefore, the average size and volume fraction of precipitates in Fig. 7(b) and (d) were calculated by the Image-Pro Plus (IPP) software, wherein the average size of precipitates was measured at 2 degree intervals passing through centroid. All parameters were measured five times and then averaged. The average size and volume fraction of precipitates in Fig. 7(b) are 119.09 nm and 0.068, and the same size parameters for precipitates in Fig. 7(d) are 39.745 nm and 0.09, respectively.

4. Discussions

The crystallization range of aluminum alloy is relatively wide; hence, coarse α-Al dendrites are first formed during solidification. The dendrites hinder the flow of eutectic liquid phase, resulting in a sharp decline of the fluidity of the semi-solidified alloy, which causes defects, including cracks and shrinkage holes (Fig. 3a), inside the casting under poor feeding conditions (Ref 17). These defects preferentially act as the source of cracks under tension, and cause premature generation of cracks.

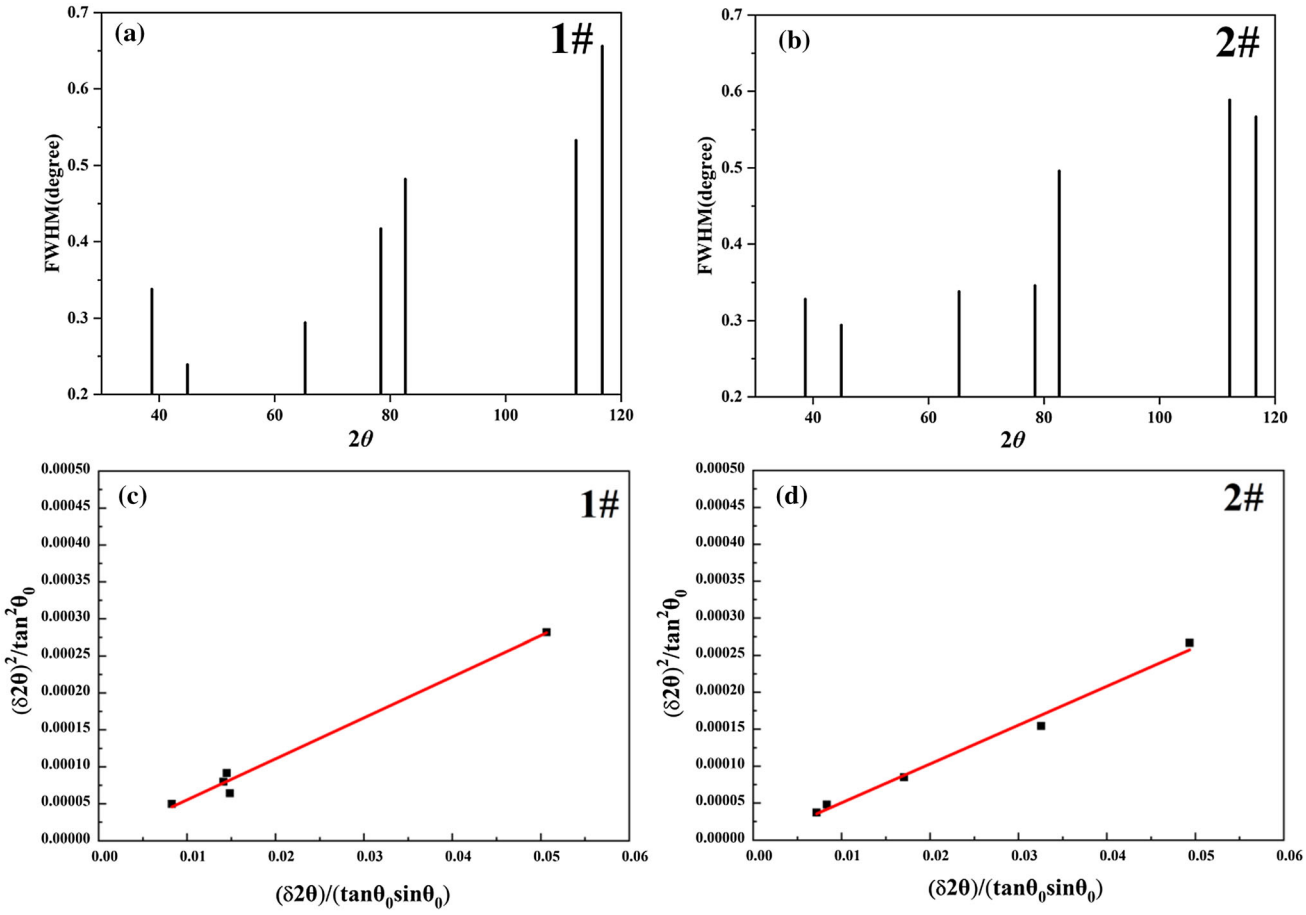

Fig. 6 XRD half peak width for (a) 1# and (b) 2# alloys and fitting relationships between $(\delta 2\theta)^2/\tan^2\theta_0$ and $(\delta 2\theta)/\tan\theta_0\sin\theta_0$ for (c) 1# and (d) 2# alloys

Table 2 Dislocation enhancement and related parameters

Samples	d/nm	$<e^2>^{1/2}(10^{-4})$	$\rho/(10^{14}\mathrm{m}^2)$	σ_ρ/MPa
1#	27.65888689	1.20167	0.52623	39.61492093
2#	29.28897338	3.03371	1.25457	61.1673047

Cracks usually propagate along the interface of different phases (Ref 18). The eutectic Si particles and IMCs in the alloy play a bridging role to facilitate the spread of micro-cracks or cracks (Ref 19). Eutectic Si particles occupy a large volume fraction in the Al-Si alloys, and their shape and size have a significant impact on the plasticity of the alloy. When the size is large, especially the irregular shape, stress concentration is likely to occur during the stress process, leading to the formation of micro-cracks. The effects of residual coarse IMCs on the mechanical properties of alloys are similar to that of the eutectic Si particles. Due to their poor deformability, the IMCs suppress the deformation of the surrounding matrix, resulting in stress concentration in the IMCs, which further leads to separation between the IMCs and matrix (i.e., a precursor to the cracks). Several cracks propagate rapidly and connect to each other inside the alloy, causing the alloy to fracture (Ref 18). According to the Griffith equation (Ref 20-22), the intrinsic fracture stress σ_f can be defined as per Eq. (4):

$$\sigma_f = \left(\frac{2E\gamma}{\pi L}\right)^{1/2} \quad \text{(Eq 4)}$$

where $L$is the length of the internal defect, E is the Young's modulus of the crystal, and γ is the fracture surface energy. For 1# alloy, the above factors corresponded to a significantly increased L value and a lower inherent fracture stress (σ_f). In other words, 1# alloy is more prone to fracture, so the tensile elongation of the 1# alloy is only 6%.

In contrast, in the case of forged Al-Si-Cu alloy, casting defects were not observed in the fracture morphology, and a significant ductile fracture was demonstrated. This result indicates that the compactness and mechanical properties of the alloy were improved after forging, and the casting defects, such as porosity and shrinkage holes, were effectively eliminated. The IMCs in 2# alloy were dramatically reduced under forging at 450 °C (Fig. 4). Han and Sjölander et al. (Ref 23, 24)

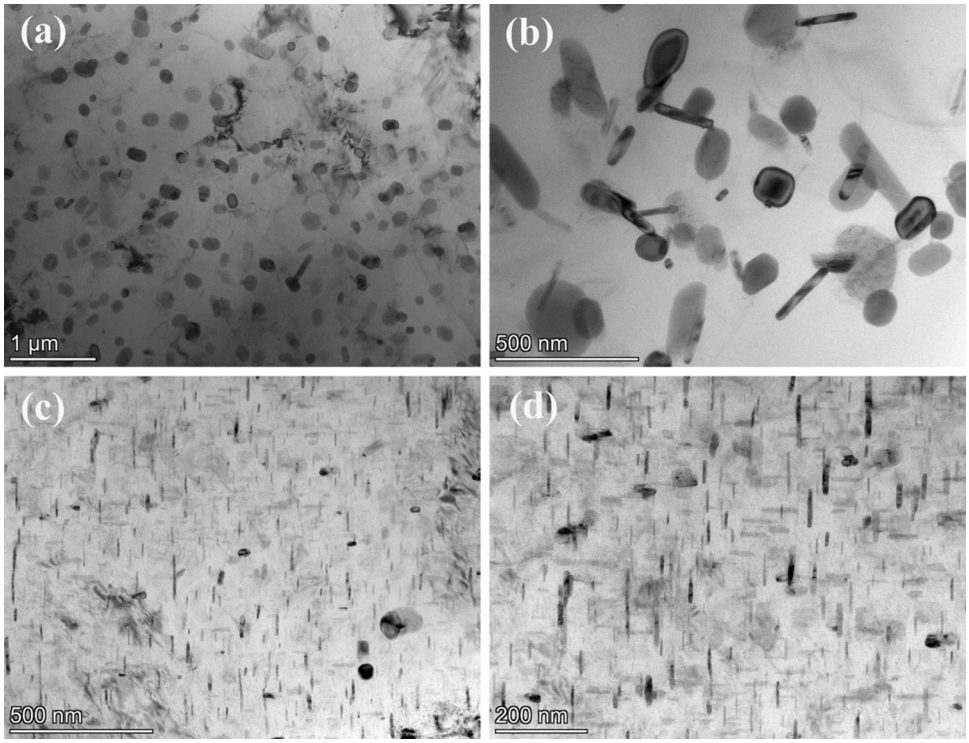

Fig. 7 TEM images of Al-Si-Cu alloys: (a) low-magnification image of 1#, (b) high-magnification image of 1#, (c) low-magnification image of 2#, and (d) high-magnification image of 2#

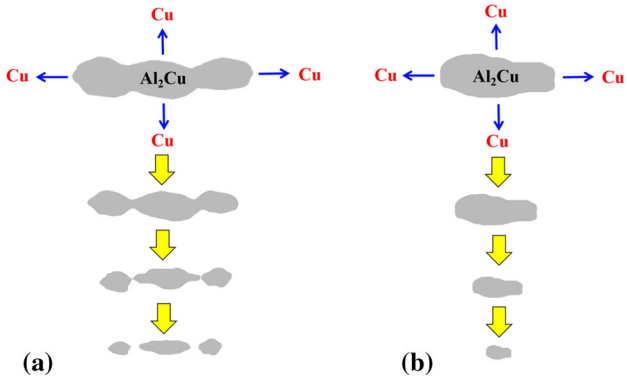

Fig. 8 Dissolution model of Al_2Cu particles: (a) eutectic Al_2Cu and (b) blocky Al_2Cu (Ref 24)

studied the dissolution of eutectic Al_2Cu phase during solution treatment. According to the specified dissolution model (Fig. 8), the blocky Al_2Cu was more difficult to dissolve than eutectic Al_2Cu phase, because the former needs to dissolve via slow diffusion. The eutectic Al_2Cu is dissolved by breaking into small pieces, which then spheroidizes into small particles, and finally, dissolve by the radial diffusion of Cu to the surrounding matrix. Forging breaks the IMCs, accelerates the diffusion and dissolution in the surrounding matrix at high temperature, and increases the supersaturation of the matrix. Also, forging process introduces a high density of dislocations and vacancies in the alloys, and 2# alloy receives dislocation strengthening effect from the entangled dislocations (Ref 25). As less activation energy is required, these crystal defects also promote the heterogeneous nucleation of GP zones (Ref 26, 27). During this process, if the GP zones reach the critical radius (depending on supersaturation), they can further form metastable precipitates θ' that are semi-coherent with the matrix; otherwise, they become unstable and re-dissolve. Lower supersaturation and/or higher temperatures usually require a larger critical radius (Ref 24). In the forged alloy, a high density of fine θ and θ' precipitates coexist (Fig. 7c, d), and the forging process further promote the precipitation kinetics of the alloy in subsequent aging.

The mechanisms of sliding dislocations and precipitation are shearing or by-passing. In general, small and low-hardness precipitates (GP zone and θ') are sheared by sliding dislocations, and the strengthening effect of the precipitates rises as their size increases (Ref 28). Due to the incoherence between the θ and Al matrix, it is difficult for the dislocations to shear θ phase only via bypassing mechanism. For the dislocation bypass mechanism, the contribution of the yield strength can be described as (Ref 29, 30):

$$\sigma\text{bypass} = \text{c2} f^{\frac{1}{2}} r^{-1} \quad \text{(Eq 5)}$$

where c_2 is a constant, f is the volume fraction of the precipitate, and r is the radius of the precipitate.

$$\text{c2} = \mu b \left(\frac{3}{2\pi}\right)^{\frac{1}{2}} \quad \text{(Eq 6)}$$

where μ = 42.5 GPa is the shear modulus mismatch between the matrix and precipitates, and b is the Burgers vector = 0.286 nm (Ref 31, 32). Therefore, equation (5) can be expressed as (Ref 30):

$$\sigma\text{bypass} = 8340 f^{\frac{1}{2}} r^{-1}. \quad \text{(Eq 7)}$$

As per quantitative volume fractions and average sizes, the yield strength contribution values of 1# and 2# alloy were calculated as 18.26 MPa and 62.95 MPa, respectively, with a difference of 44.69 MPa. This calculated result is roughly consistent with the yield strength difference between 1# and 2# alloy (yield strength of 1# and 2# alloy were 133.34 MPa and 187.57 MPa, respectively). It also indicated that the yield strength improves with the increased volume fraction of the precipitates and is inversely proportional to the radius of the precipitates. With size coarsening and decrease in quantity of the precipitates, the strengthening effect gradually reduces (Ref 33–35). Therefore, dense θ' and θ precipitates are vital for the enhanced strength of 2# alloy, while the coarsening of stable precipitations led to strength reduction for 1# alloy.

Kyuhong Lee et al. (Ref 19) concluded that in the as-cast and forged A356 alloy, the eutectic Si particles are spheroidized, and the modified eutectic Si particles tend to be rearranged uniformly. A similar phenomenon was also observed in Fig. 4(d) and (e). The spheroidized and rearranged eutectic Si can greatly inhibit the premature generation and propagation of cracks and further improve the elongation and fracture toughness of the forged alloy.

5. Conclusions

Herein, the Al-9Si-5Cu-0.2Zr-0.1Sr-0.16Ti-0.1Ce aluminum alloy was developed and the effect of forging on the microstructure and mechanical properties of the alloy was investigated. The following conclusions can be drawn.

The microstructure of cast Al-9Si-5Cu alloy was primarily composed of irregular Si-eutectic and IMCs. After aging, the cast alloy precipitated sparse θ phases. The casting defects and irregular Si-eutectic and IMCs led to premature initiation and accelerating of crack propagation, and the elongation of cast alloy was only 6%.

In contrast, in the case of forged alloy, the casting defects were effectively eliminated and the irregular Si-eutectic were spheroidized. The coarse IMCs were broken by the forging process and gradually dissolved in the Al matrix during subsequent solution treatment. High temperature forging further promoted precipitation kinetics of the alloy in subsequent aging, so that dense fine θ and θ' strengthening phases coexisted and distributed uniformly. Moreover, the dislocation strengthening effect for the forged alloy was enhanced. Owing to the precipitation and dislocation strengthening mechanisms, the mechanical properties including the yield strength, tensile strength and hardness were improved. By optimizing the microstructure of the alloy, forging inhibited the premature initiation and propagation of cracks, and the elongation and fracture toughness of the forged Al-9Si-5Cu alloy significantly increased to 14%.

Acknowledgments

Thanks to the financial supports from the Key Projects of Equipment Pre-research Foundation of the Ministry of Equipment Development of the Central Military Commission of China (No: 6140922010201) and the Key Projects of Research and Development of Zhenjiang (GY2018021).

References

1. H. Peng, C. Chen, H.Y. Zhang et al., Recent Development of Improved Clinching Process, *Int. J. Adv Manuf. Technol.*, 2020, **110**, p 1–31
2. R. Yi, C. Chen, Y. Li et al., The Bonding Between Glass and Metal, *Int. J. Adv Manuf. Technol.*, 2020, **111**, p 1–21
3. C. Chen, H.Y. Zhang, Y.Q. Xu et al., Investigation of the Flat-Clinching Process for Joining Three-Layer Sheets on Thin-Walled Structures, *Thin Wall Struct.*, 2020, **157**, p 107034
4. B. Donadoni, G.L.D. Gouveia, A. Garcia et al., A Comparison of Experimental Time-Secondary Dendritic Spacing and Coarsening Models for Al-Si-Cu Alloys, *J. Manuf. Process.*, 2020, **54**, p 14–18
5. J.D. Poplawsky, B.K. Milligan, L.F. Allard et al., The Synergistic Role of Mn and Zr/Ti in Producing $\theta'/L1_2$ Co-precipitates in Al-Cu Alloys, *Acta Mater.*, 2020, **194**, p 577–586
6. A.K. Jha and S.N. Ojha, Deformation Behavior of Aluminum-Silicon (Al-Si) Alloy During Forging Under Various Processing Conditions, *Mater. Today Proc.*, 2018, **5**, p 26955–26960
7. C.G. Kang and J.S. Choi, Effect of Gate Shape and Forging Temperature on the Mechanical Properties in the Injection Forging Process of Semi-solid Aluminum Material, *J. Mater. Process. Technol.*, 1998, **73**, p 251–263
8. C.G. Kang, J.S. Choi et al., The Effect of Strain Rate on Macroscopic Behavior in the Compression Forming of Semi-solid Aluminum Alloy, *J. Mater. Process. Technol.*, 1999, **88**, p 159–168
9. F.F. Wu, S.T. Li, G.A. Zhang et al., Microstructural Evolution and Mechanical Properties of Hypereutectic Al-Si Alloy Processed by Liquid Die Forging, *Bull. Mater. Sci.*, 2014, **37**, p 1153–1157
10. P. Luo, D.T. Mcdonald, W. Xu et al., A Modified Hall-Petch Relationship in Ultrafine-Grained Titanium Recycled from Chips by Equal Channel Angular Pressing, *Scr. Mater.*, 2012, **66**, p 785–788
11. C.Y. Zhu, X.J. Xu, H. Wang et al., Effect of Mg on Microstructure and Properties of Al-8.95Zn-(1.9–2.6)Mg-1.18Cu-0.44Zr Rolled Aluminum Alloy, *Mater. Res. Express*, 2018, **5**, p 065803
12. X.J. Xu, H.H. Shao, J. Gao et al., Effect of Sic Film on Tensile Properties of Nanostructured Ti Produced by Compressive Deformation at Liquid-Nitrogen Temperature, *Mater. Sci. Eng. A*, 2008, **493**, p 195–201
13. K.M. Youssef, R.O. Scattergood, K.L. Murty et al., Nanocrystalline Al-Mg Alloy with Ultrahigh Strength and Good Ductility, *Scr. Mater.*, 2006, **54**, p 251–256
14. S.C. Wang and M.J. Starink, Precipitates and Intermetallic Phases in Precipitation Hardening Al-Cu-Mg-(Li) Based Alloys, *Int. Mater. Rev.*, 2005, **50**, p 193–215
15. S.K. Varma, D. Salas, E. Corral et al., Microstructural Development During Aging of 2014 Aluminum Alloy Composite, *J. Mater. Sci.*, 1999, **34**, p 1855–1863
16. M. Okayasu and S. Go, Precise Analysis of Effects of Aging on Mechanical Properties of Cast ADC12 Aluminum Alloy, *Mater. Sci. Eng. A*, 2015, **638**, p 208–218
17. A. Reis, Z. Xu, R.V. Tol et al., Modelling Feeding Flow Related Shrinkage Defects in Aluminum Castings, *J. Mater. Process. Technol.*, 2012, **14**, p 1–7
18. Y. Cao, X. Chen, Z. Wang et al., Effect of Cd Micro-addition on Microstructure and Mechanical Properties in Ternary Al-Si-Cu Alloy, *J. Alloys Compd.*, 2020, **851**, p 156739
19. K. Lee, Y.N. Kwon and S. Lee, Effects of Eutectic Silicon Particles on Tensile Properties and Fracture Toughness of A356 Aluminum Alloys Fabricated by Low-Pressure-Casting, Casting-Forging, and Squeeze-Casting Processes, *J. Alloys Compd.*, 2008, **461**, p 532–541
20. C.L. Xu, H.Y. Wang, Y.F. Yang et al., Effect of Al-P-Ti-TiC-Nd_2O_3 Modifier on the Microstructure and Mechanical Properties of Hypereutectic Al-20 wt.%Si Alloy, *Mater. Sci. Eng. A*, 2007, **452**, p 341–346
21. Q. Li, T. Xia, Y. Lan et al., Effects of Rare Earth Er Addition on Microstructure and Mechanical Properties of Hypereutectic Al-20% Si Alloy, *J. Alloys Compd.*, 2013, **588**, p 97–102
22. C. Liang, Z.H. Chen, Z.Y. Huang et al., Optimizing Microstructures and Mechanical Properties of Hypereutectic Al-18%Si Alloy via Manipulating its Parent Liquid State, *Mater. Sci. Eng. A*, 2017, **690**, p 387–392
23. Y.M. Han, A.M. Samuel, F.H. Samuel, S. Valtierra and H.W. Doty, Effect of Solution Heat Treatment Type on the Dissolution of Copper Phases in Al-Si-Cu-Mg Type Alloys, *AFS Trans.*, 2008, **116**, p 79–90

24. E. Sjölander and S. Seifeddine, The Heat Treatment of Al-Si-Cu-Mg Casting Alloys, *J. Mater. Process. Technol.*, 2010, **210**, p 1249–1259
25. E. Feyzullahoglu, A.T. Ertürk and E.A. Güven, Influence of Forging and Heat Treatment on Wear Properties of Al-Si and Al-Pb Bearing Alloys in Oil Lubricated Conditions, *Trans. Nonferr. Met. Soc.*, 2013, **23**, p 3575–3583
26. A.M. Cassell, J.D. Robson, C.P. Race et al., Dispersoid Composition in Zirconium Containing Al-Zn-Mg-Cu (AA7010) Aluminium Alloy, *Acta Mater.*, 2019, **169**, p 135–146
27. Y. Wang, G. Zhao, X. Xu et al., Microstructures and Mechanical Properties of Spray Deposited 2195 Al-Cu-Li Alloy Through Thermo-mechanical Processing, *Mater. Sci. Eng. A*, 2018, **727**, p 78–89
28. S.K. Shaha, F. Czerwinski, W. Kasprzak et al., Ageing Characteristics and High-Temperature Tensile Properties of Al-Si-Cu-Mg Alloys with Micro-additions of Mo and Mn, *Mater. Sci. Eng. A*, 2017, **684**, p 726–734
29. Y.Z. Hou, L. Chen, Z.G. Li et al., Effects of Artificial Aging on Microstructure, Mechanical Properties and Stress Corrosion Cracking of a Novel High Strength 7A99 Al Alloy, *Mater. Sci. Eng. A*, 2020, **780**, p 139217
30. D. Pan, L. Xian, Y. Yang et al., Nano-scale Precipitate Evolution and Mechanical Properties of 7085 Aluminum Alloy During Thermal Exposure, *Mater. Sci. Eng. A*, 2018, **729**, p 411–422
31. B.M. Christopher, C.D. David and N.S. David, Coarsening Resistance at 400 °C of Precipitation-Strengthened Al-Zr-Sc-Er Alloys, *Acta Mater.*, 2001, **59**, p 7029–7042
32. C. Schlesier and E. Nembach, Strengthening of Aluminum-Lithium Alloys by Long-Range Ordered δ' Precipitates, *Acta Metall. Mater.*, 1995, **43**(3983), p 3990
33. A. Shyam, S. Roy, D. Shin et al., Elevated Temperature Microstructural Stability in Cast AlCuMnZr Alloys Through Solute Segregation, *Mater. Sci. Eng. A*, 2019, **765**, p 138279
34. S. Roy, L.F. Allard, A. Rodriguez et al., Comparative Evaluation of Cast Aluminum Alloys for Automotive Cylinder Heads: Part II-Mechanical and Thermal Properties, *Metall. Mater. Trans. A*, 2017, **48**, p 2543–2562
35. B.K. Milligan, S. Roy, C.S. Hawkins et al., Impact of Microstructural Stability on the Creep Behavior of cast Al-Cu Alloys, *Mater. Sci. Eng. A*, 2020, **772**, p 138697

Publisher's Note Springer Nature remains neutral with regard to jurisdictional claims in published maps and institutional affiliations.